Dirac states in the noncentrosymmetric superconductor BiPd

Arindam Pramanik,[1] Ram Prakash Pandeya,[1] Denis V. Vyalikh,[2,3] Alexander Generalov,[4] Paolo Moras,[5] Asish K. Kundu,[5] Polina M. Sheverdyaeva,[5] Carlo Carbone,[5] Bhanu Joshi,[1] A. Thamizhavel,[1] S. Ramakrishnan,[1] and Kalobaran Maiti[1,*]

[1]*Department of Condensed Matter Physics and Materials Science, Tata Institute of Fundamental Research, Homi Bhabha Road, Colaba, Mumbai - 400005, India*

[2]*Donostia International Physics Center (DIPC), 20018 Donostia San Sebastián, Basque Country, Spain*

[3]*IKERBASQUE, Basque Foundation for Science, 48013, Bilbao, Spain*

[4]*MAX IV Laboratory, Lund University, PO Box 118, 22100, Lund, Sweden*

[5]*Istituto di Struttura della Materia, Consiglio Nazionale delle Ricerche, I-34149 Trieste, Italy*

(Received 12 September 2020; revised 18 March 2021; accepted 22 March 2021; published 1 April 2021)

Quantum materials having Dirac fermions in conjunction with superconductivity is believed to be the candidate material to realize exotic physics as well as advanced technology. Angle-resolved photoemission spectroscopy (ARPES), a direct probe of the electronic structure, has been extensively used to study these materials. However, experiments often exhibit conflicting results on dimensionality and momentum of the Dirac fermions (e.g., Dirac states in BiPd, a novel noncentrosymmetric superconductor), which is crucial for the determination of the symmetry, time-reversal invariant momenta, and other emerging properties. Employing high-resolution ARPES at varied conditions, we demonstrated a methodology to identify the location of the Dirac node accurately and discover that the deviation from two dimensionality of the Dirac states in BiPd proposed earlier is not a material property. These results helped to reveal the topology of the anisotropy of the Dirac states accurately. We have constructed a model Hamiltonian considering higher-order spin-orbit terms and demonstrate that this model provides an excellent description of the observed anisotropy. Intriguing features of the Dirac states in a noncentrosymmetric superconductor revealed in this study are expected to have significant implications regarding the properties of topological superconductors.

DOI: 10.1103/PhysRevB.103.155401

I. INTRODUCTION

Recent times have seen the emergence of a new class of insulating materials, which are topological in nature. While the bulk of these materials is insulating, the surface harbours partially filled (metallic) spin-split two-dimensional bands with conelike structure (Dirac cone) arising due to the topological nature of the bulk bands. Bi_2Se_3 is one of the most studied materials in this category [1], where the surface states and its evolution with impurities have been studied extensively [2–4]. The pool of topological materials have been enriched via discovery of Dirac fermions as the surface states in superconductors such as BiPd [5–7], β-$PdBi_2$ [8], $Cu_xBi_2Se_3$ [9], $Sr_xBi_2Se_3$ [10,11], etc. Among these topological materials, BiPd grabbed much attention, as it stabilizes in noncentrosymmetric monoclinic structure ($P2_1$) known as α-BiPd, and superconductivity appears below 3.8 K [12–14]. Above 483 K, it undergoes a polymorphic transition from α-BiPd to orthorhombic β-BiPd (space group $Cmc2_1$).

Due to the absence of inversion symmetry, the (010) and $(0\bar{1}0)$ faces of BiPd are inequivalent, and the binding energy at the Dirac nodes on respective faces are also different. Interestingly, the twinning in the samples allows photoemission experiments to capture properties of both surfaces simultaneously; while the Dirac bands on the (010) face appear clearly in the experimental spectra, bands on the $(0\bar{1}0)$ face are often weak and appear in the immediate vicinity of the bulk states. Benia *et al.* [5] pointed out that the Dirac states in BiPd may not have topological origin, as these are found in density functional calculations, both with and without spin-orbit (SO) coupling. On the other hand, spin-resolved photoemission measurements have confirmed the spin polarization of these states, which is a signature of topological behavior [7]. It is of note here that spin-polarized surface states are also observed in systems with heavy elements due to strong Rashba coupling.

Despite several studies, even the identification of the location of a Dirac node and the dimensionality of the Dirac states are outstanding issues. Thirupathaiah *et al.* [6] reported this band to be found at $\bar{\Gamma}$ (Brillouin zone center). However, Yaresko *et al.* have shown the Dirac states to be positioned at $\bar{S}$, a high-symmetry point at the surface Brillouin zone boundary based on their detailed density functional theoretical (DFT) calculations [15]. In addition to the conflicting results regarding the location of the Dirac node, Thirupathaiah *et al.* [6] proposed the three-dimensional nature of the Dirac states depicted by an energy gap at the Dirac node varying with k_z, although the repetitive nature of the gap as a function of k_z was not observed. However, the DFT results characterize Dirac states as two-dimensional surface states [5,7]. We carried out high-resolution angle-resolved photoemission

*Corresponding author: kbmaiti@tifr.res.in

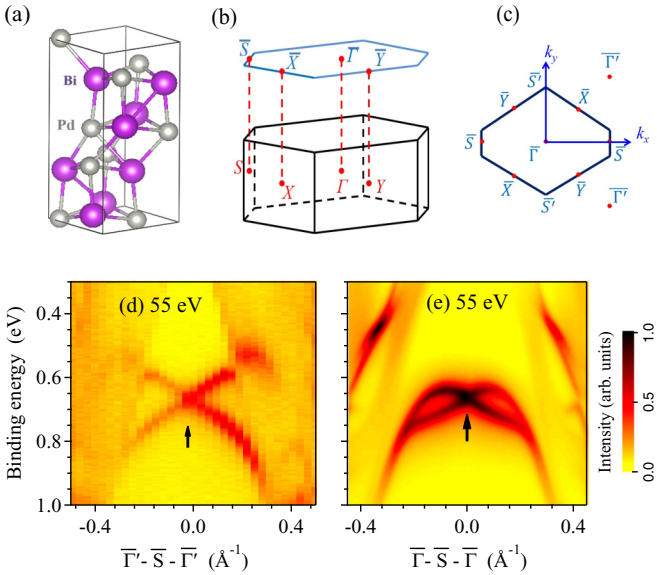

FIG. 1. (a) Unit cell of BiPd in real space. (b) Bulk and (c) surface Brillouin zones. ARPES data (d) along $\overline{\Gamma}' - \overline{S} - \overline{\Gamma}'$ and (e) $\overline{\Gamma} - \overline{S} - \overline{\Gamma}$ vectors. The Dirac point is identified with an arrow, and the k axis is shifted to make the $\overline{S}$ point zero.

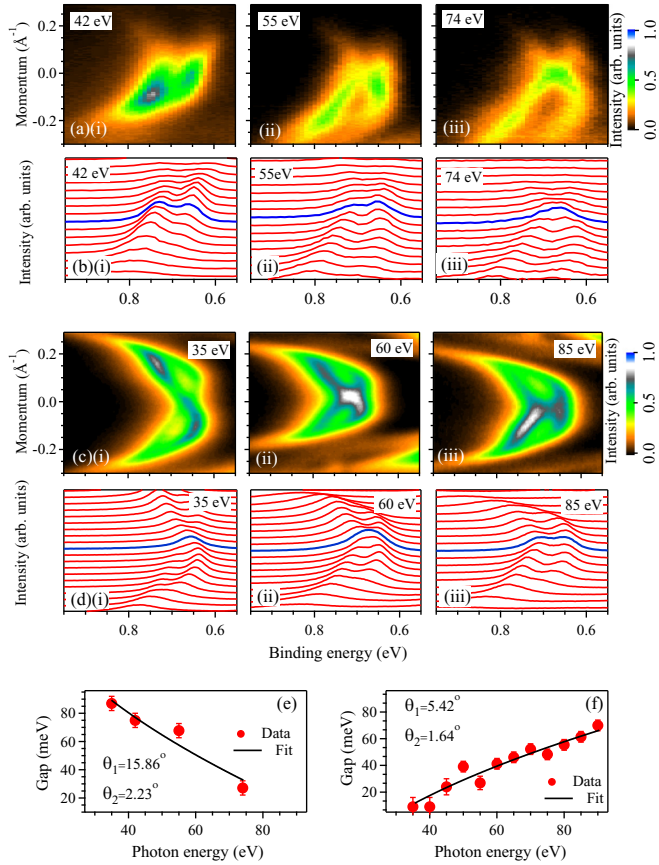

FIG. 2. (a)(i)–(iii) ARPES data collected along $\overline{\Gamma} - \overline{S} - \overline{\Gamma}$ direction and (b)(i)–(iii) the corresponding energy distribution curves (EDCs) after normalizing the sample position using 74-eV photon energy. (c)(i)–(iii) A similar second set of ARPES data collected after sample normalization using 35-eV photon energy and (d)(i)–(iii) corresponding EDCs. Blue lines mark the EDCs passing through the Dirac node. The energy gaps derived at the Dirac node at the $\overline{S}$ point from (e) the first and (f) the second set of the spectra. Black lines superimposed over the data points represent the estimated energy gaps considering the $\overline{\Gamma} - \overline{S}$ vector makes an azimuthal angle θ_1 and tilt angle θ_2, as shown in the Appendix.

spectroscopic (ARPES) measurements at carefully chosen experimental conditions and discover that the Dirac states are truly two dimensional; the anomalies reported earlier arose due to the sample alignment used in those experiments. Furthermore, we find that the anisotropy in the dispersion of the Dirac bands reported earlier [5,6] appears far away from the Dirac node. We have constructed a model Hamiltonian considering higher-order spin-orbit terms, which provides a good description of all the features of the Dirac bands observed experimentally.

II. EXPERIMENT

High-quality single crystals of BiPd were grown using a modified Bridgman method. The crystal structure of the sample was determined via analysis of the powder x-ray diffraction pattern, and good crystallinity has been ensured employing Laue diffraction experiments. The lattice parameters found in the study correspond to the monoclinic structure as reported elsewhere [12]. Magnetization measurements exhibit a superconducting transition at 3.8 K. ARPES measurements were performed at Diamond Light Source, United Kingdom, and Elettra, Italy. At the Diamond Light Source, experiments were carried out at the I05 beamline [16] at a temperature of 10 K, base pressure of 5×10^{-11} Torr, and energy resolution of 5 meV. Measurements at Elettra were done at the VUV beamline at a temperature of 25 K, base pressure of 6×10^{-11} Torr, and energy resolution of 10 meV.

III. RESULTS AND DISCUSSION

The crystal unit cell of BiPd is shown in Fig. 1(a), exhibiting a noncentrosymmetric structure. In Figs. 1(b) and 1(c), we show the bulk Brillouin zone (BZ) and its projection on the surface, respectively. The axis system is defined by aligning k_x along the $\overline{\Gamma}$-$\overline{S}$ direction and k_y along the $\overline{\Gamma}$-$\overline{S}'$ direction. Photoemission spectra along two directions are shown in Figs. 1(d) and 1(e), with the Dirac point appearing at 0.66-eV binding energy shown using an arrow. The analysis of the data as discussed in Fig. 2 suggests that the Dirac point is positioned at the $\overline{S}$ point in the surface Brillouin zone, which is about 0.73 Å^{-1} away from the $\overline{\Gamma}$ point; in the figure, the k axis is shifted to make it zero at the Dirac node. While the bands along $\overline{\Gamma}' - \overline{S} - \overline{\Gamma}'$ exhibit spin splitting varying monotonically with momentum, the momentum dependence of the spin splitting along $\overline{\Gamma} - \overline{S} - \overline{\Gamma}$ is nonlinear; it increases to a maximum near a momentum of 0.1 Å^{-1} away from $\overline{S}$ and then decreases, revealing strong anisotropy of the Dirac fermionic bands as discussed earlier [5,6].

To investigate the dimensionality of the Dirac states, we acquired spectra at various photon energies, which helps to decide the surface or bulk nature of the bands. In Figs. 2(a)(i)–2(a)(iii), we show a set of spectra along with corresponding

energy distribution curves (EDCs) in Figs. 2(b)(i)–2(b)(iii). The second set of spectra is displayed in Figs. 2(c)(i)–2(c)(iii) with corresponding EDCs in Figs. 2(d)(i)–2(d)(iii). Pieces cut from the same single crystal were used to obtain these two sets of spectra. A close inspection reveals interesting differences between the two sets. In the first set (the sample position optimized using 74-eV photon energy), as the photon energy is lowered, the Dirac cone becomes more asymmetric and the bands do not cross each other. The energy gap at the Dirac node was derived by fitting two peaks in the EDC [blue curves in Figs. 2(b)] across the node. The gap increases as the probing energy is lowered. The second set of the spectra were collected after optimizing the sample position at 35-eV photon energy, and the Dirac node could be captured just by optimization of the sample alignment. Curiously, the second set exhibits an opposite trend of the gap at the Dirac node; the energy gap continuously increases with the increase in photon energy across 74 eV, as manifested clearly in the EDCs [blue curves in Figs. 2(d)]. In this case, the dispersion of the Dirac bands remains symmetric over the energy range studied. In Figs. 2(e) and 2(f), we show the derived energy gaps of the first and second sets, respectively, exhibiting an opposite trend. We note here that the Dirac bands shown in Figs. 1(d) and 1(e) collected at 55-eV photon energy after optimizing the sample position also show a distinct Dirac node. All these results suggest that the k point at the Dirac node may be different from the $\overline{\Gamma}$ point; the change in photon energy moves the k point away from the Dirac node.

In order to probe this further, we consider that the $\overline{\Gamma} - \overline{S}$ vector makes an azimuthal angle, θ_1, with the vertical axis and tilt angle, θ_2; here the photoemission plane is a horizontal plane as shown in the Appendix. Clearly, the presence of finite θ_1 will manifest as an asymmetry in the cone structure as the probed k vector does not pass through the Dirac node. This argument is verified from the values of θ_1 obtained from fittings in Figs. 2(e) and 2(f); the first set of spectra [see Fig. 2(a)] exhibit strong asymmetry and could be captured with a higher value of θ_1 compared to the second set shown in Fig. 2(b). Derived values of θ_2 are also listed in the figures. Excellent representation of the experimental results establishes that the gap at the Dirac node is not the property of the material but arises due to the sample alignment and that the Dirac node is not located at $\overline{\Gamma}$. A zero gap within the experimental error can be obtained for both sets of data at all probing energies once the fitted curve is subtracted from the measured gap. This is manifested in the experimental data; the sample realignment at different photon energies leads to reduction of the energy gap to zero. For example, the data in Figs. 1(d) and 1(e) exhibit a distinct Dirac node for photon energy of 55 eV, although the spectra collected using the other setup for the same photon energy show a nonzero gap. This is in addition to the data in Figs. 2(a)(iii) and 2(c)(i) for 74 and 35 eV, respectively. This establishes the finite momentum at the Dirac node and two-dimensional nature of the Dirac states, as there is no observable variation of the bands with the photon energy.

Identification of the correct momentum and dimensionality of the Dirac node is important, as the symmetry of the states depends on the momentum of the Dirac states, and dimensionality provides the behavior of the states. For the ease of presentation and/or calculations, sometimes, a nonprimitive

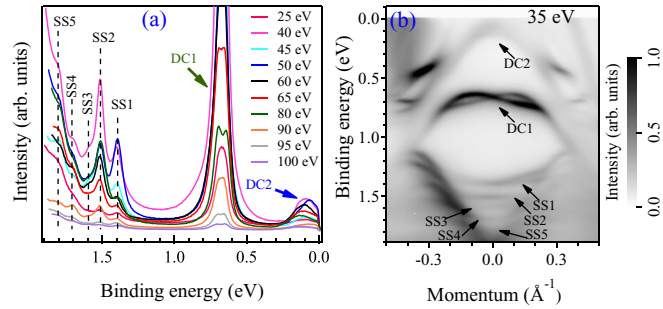

FIG. 3. (a) EDCs passing through the Dirac node are plotted for multiple photon energies ranging from 25 to 100 eV. DC1 and DC2 are the Dirac cones on 010 and $0\bar{1}0$ surfaces, respectively. DC1 exhibits splitting into two peaks where the alignment of the sample is away from the $\overline{S}$ point due to the change in photon energy. SS1–SS5 label the surface states at higher binding energies. (b) A representative spectrum at 35 eV shows all the observed surface states of BiPd.

unit cell is used to derive the electronic structure of a system. Such consideration introduces additional folding of the energy bands, and one needs to unfold them to identify their momentum as discussed earlier [15]. On the experimental front, the way to identify the correct momentum and dimensionality of the eigenstates is to map the Fermi surface at multiple photon energies, presumably at photon energies corresponding to a nonequivalent k point, and then take the correct cut. The experimental data and ensuing analysis presented here provide the momentum and dimensionality of the Dirac fermions consistent with the theoretical results [15].

Besides the widely discussed Dirac states, we discover a few more two-dimensional states lying at higher binding energies. In Fig. 3(a) we show the EDCs at various photon energies taken across the Dirac node. DC1 is the Dirac state under investigation. DC2 is the Dirac cone on the $(0\bar{1}0)$ surface [5]. In addition, a few other states labeled SS1–SS5 are seen to be positioned at fixed binding energies even as the photon energy is varied over a large range. Since these bands are not observed in the theoretical results [15] for the bulk band structure, we attribute these two-dimensional states as surface states. Understanding of the nature of these bands requires further theoretical studies, including various surface effects.

We now address the issue of anisotropy of the Dirac bands; such anisotropy has also been reported in other materials. For example, Bi_2Te_3 [17,18] and Bi_2Se_3 [19,20] are two prominent cases of this class. There are other cases, too, such as Ru_2Sn_3 [21], β-Bi_4I_4 [22], β-HgS [23], β-Ag_2Te [24], Au film grown on Ag(111) [25], Ag film grown on Au (111) [25], etc. Anisotropy in these systems is attributed to the symmetries at the surfaces. In Figs. 4(a)–4(d) we show the constant-energy contours of BiPd taken across the Dirac states. Energy positions of the contours are shown using schematics in Figs. 4(e) and 4(f) with dashed lines. Each constant-energy map consists of two contours. Green and red colors are used to identify the contours with the energy bands above and below the Dirac point. The shape of all the contours exhibits the twofold rotational symmetry of the crystal belonging to a C_2 point group. Interestingly, the inner contour near the nodal point is isotropic (cut A, B, and C) and

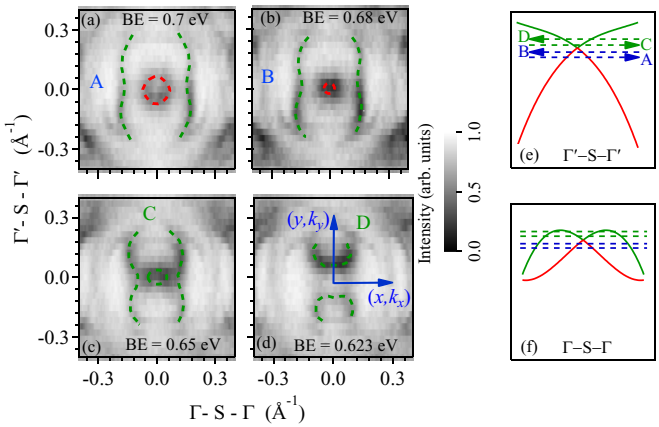

FIG. 4. Constant-energy contours in the x-y plane at binding energies (a) 0.7 eV, (b) 0.68 eV, (c) 0.65 eV, and (d) 0.623 eV obtained from the ARPES data at 55-eV photon energy, as shown in Fig. 1. The binding energy positions of the contours are labeled A, B, C, and D and are shown schematically in (e) along the k vector $\overline{\Gamma}' - \overline{S} - \overline{\Gamma}'$ and (f) along the k vector $\overline{\Gamma} - \overline{S} - \overline{\Gamma}$. Green and red colors identify the contours derived from the green- and red-colored energy bands. The Cartesian coordinate system is shown in (d); (x, k_x) lies along $\overline{\Gamma} - \overline{S} - \overline{\Gamma}$.

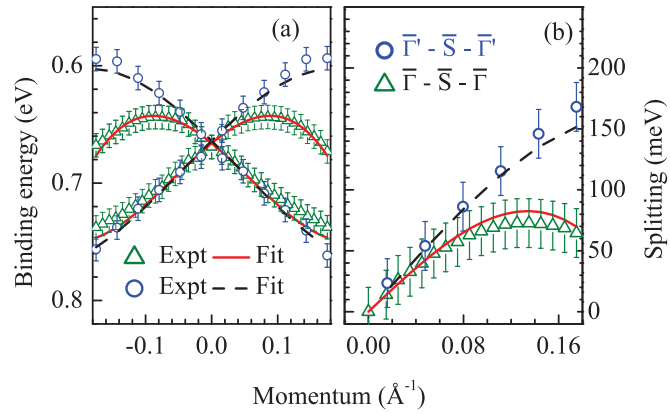

FIG. 5. (a) Dispersion along $\overline{\Gamma}' - \overline{S} - \overline{\Gamma}'$ (blue open circles) and $\overline{\Gamma} - \overline{S} - \overline{\Gamma}$ (green open triangles) derived from EDCs. Solid and dashed lines represent the fits based on the eigenvalue equation (1). (b) Spin splitting along $\overline{\Gamma} - \overline{S} - \overline{\Gamma}$ (green open triangles) and $\overline{\Gamma}' - \overline{S} - \overline{\Gamma}'$ (blue open circles). Solid and dashed lines represent the fits based on the eigenvalue equation (1).

gradually evolves into a twofold symmetric curve far away from the nodal point. At the top of the Dirac cone, the contour evolves into two disjoint segments (cut D). Further, we notice that the top and bottom portions of the outer contour (green) are missing in all the cuts including D. This scenario is consistent with the observation in Fig. 1(d) where the surface bands merge with the bulk band along $\overline{\Gamma}' - \overline{S} - \overline{\Gamma}'$, resulting in an incomplete contour. The twofold rotational symmetry implies that electrons are subject to the effects of crystal potential. Benia *et al.* argued that a twofold rotational symmetry in the Rashba coupling strength at the surface is responsible for this anisotropic band dispersion [5]. However, it is difficult to capture the nonparabolic dispersion along $\overline{\Gamma} - \overline{S} - \overline{\Gamma}$ [Fig. 1(e)] as well as the contour shapes shown in Fig. 4 using this scenario. Moreover, a C_2 symmetric Rashba coupling, which is first order in momentum (k_x, k_y), will produce twofold symmetric contours near the node, unlike the circular contours seen here.

Experimentally observed dispersions of the Dirac bands along two orthogonal directions are shown in Fig. 5(a). It is evident in the figure that although the dispersions are different far away from the node they are very similar near the node, as found in the constant-energy contours of Fig. 4. Such a behavior suggests importance of higher-order spin-orbit terms [26,27]. Considering the C_2 point group of the material and time-reversal symmetry, we derive the Hamiltonian up to the third-order term in momentum. The choice of the axes are shown in Fig. 1, where the x axis lies along the $\overline{\Gamma} - \overline{S} - \overline{\Gamma}$ direction. A model Hamiltonian with the $\overline{S}$ point as the reference point is constructed as follows:

$$H = A(\vec{k})\sigma_x + B(\vec{k})\sigma_y + C(\vec{k})\sigma_z + D(\vec{k})I_{2\times 2}, \qquad (1)$$

where σ_x, σ_y, and σ_z are Pauli matrices and $I_{2\times 2}$ is a 2×2 identity matrix. A, B, C, and D are functions of lattice momenta, k_x and k_y, with the following forms:

$$A(\vec{k}) = c_1 k_x + c_2 k_y + c_3 k_x k_y^2 + c_4 k_y k_x^2 + c_5 k_x^3 + c_6 k_y^3$$

$$B(\vec{k}) = c_7 k_x + c_8 k_y + c_9 k_x k_y^2 + c_{10} k_y k_x^2 + c_{11} k_x^3 + c_{12} k_y^3$$

$$C(\vec{k}) = 0$$

$$D(\vec{k}) = E_0 + c_{13} k_x^2 + c_{14} k_y^2 + c_{15} k_x k_y.$$

Clearly, for small k values, contributions from higher-order terms become insignificant and one can get essentially an isotropic description from the above Hamiltonian. By fitting the band dispersions along various k directions, one can estimate the parameters adequately to derive the band structure [28]. We discuss a typical case below.

Band dispersion and spin splitting extracted from EDCs from the spectrum at 55 eV are shown by symbols in Figs. 5(a) and 5(b), respectively. Spin splitting along the $\overline{S} - \overline{\Gamma}'$ direction is represented by open circles, and along the $\overline{S} - \overline{\Gamma}$ direction, it is open triangles. The spin splitting along $\overline{S} - \overline{\Gamma}'$ varies almost linearly with momentum, as expected for Rashba split parabolic bands. Along $\overline{S} - \overline{\Gamma}$, away from the $\overline{S}$ point, the bands deviate from the expected parabolic dispersion. The splitting varies linearly with momentum close to the $\overline{S}$ point, and at large momentum the effect of higher order takes over. Fitting of all the curves is done using expressions derived from Eq. (1) and in each case, good quality of fitting is achieved for the momentum region away from the influence of bulk bands.

To confirm that the obtained description reproduces the experimental results shown in Fig. 4, we simulated the constant-energy maps using the above description. In Fig. 6 we show the contours at binding energies similar to those shown in Fig. 4. Note that since the size of the model Hamiltonian is 2×2, it describes only the spin-split Dirac-like states and does not capture the merger of the Dirac states with the bulk bands along the $\overline{S} - \overline{\Gamma}'$ direction. Hence it provides closed contours, as expected for surface states in a scenario where merging to the bulk bands is absent. The shapes of

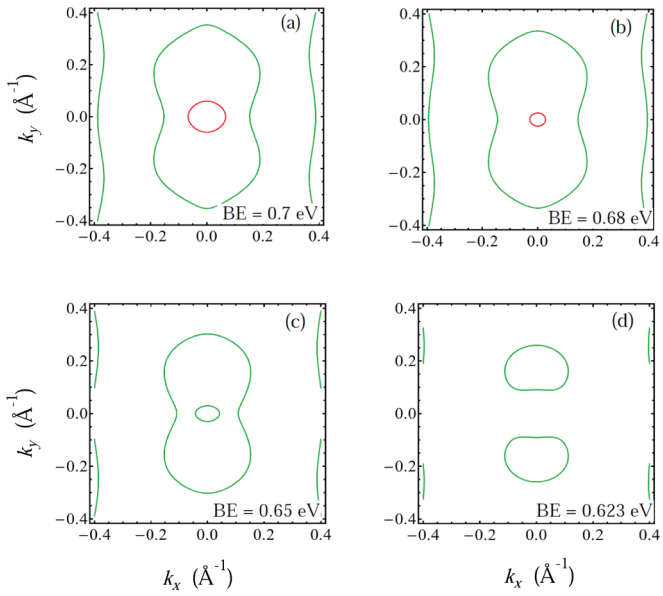

FIG. 6. Contours simulated at (a) 0.7 eV, (b) 0.68 eV, (c) 0.65 eV, and (d) 0.623 eV binding energies using the Hamiltonian in Eq. (1). Parameters used for the simulations are listed in [28]. Colors (red or green) of contours are in accordance with Fig. 4.

the contours provide an excellent description of the experimentally observed scenario around the $\overline{S}$ point. Note here that spin-orbit coupling in the solid can have contributions [$= -\frac{e\hbar}{(2mc)^2}\sigma(E(r) \times p)$, where $E(r)$ is the electric field] in addition to the atomic values. This is more so in a material having no center of symmetry, as reported earlier [29]. Thus the origin of the above behavior may be attributed to the strong spin-orbit coupling in this noncentrosymmetric solid, BiPd.

It has been shown that higher-order spin-orbit coupling gives rise to out-of-plane spin polarization in systems such as Bi_2Se_3 [26,30], Bi_2Te_3 [18,26], β-Ag_2Te [24], etc. The surface states in BiPd will, however, not possess an out-of-plane spin component. The spin-splitting term containing σ_z, which leads to the out-of-plane spin polarization, is absent in the Hamiltonian [see Eq. (1)] owing to the C_2 symmetry of the system. Hence the spin polarization of the states will lie in the k_x-k_y plane [31].

IV. CONCLUSIONS

In summary, we studied the Dirac states in a noncentrosymmetric superconductor, BiPd. The high quality of the sample and high resolution of the ARPES technique employed in this study helped to reveal subtle features in the electronic structure. Our experimental results helped to identify the momentum of the Dirac node and establish the two-dimensional character of the Dirac states, resolving the outstanding disputes on these two issues. This study brings out the importance of deriving correct experimental geometry to reveal experimental results related to the properties of materials, in particular, the cases where the point of interest is not the center of the Brillouin zone ($\overline{\Gamma}$ point). This is crucial for the identification of the symmetry properties, time-reversal invariant momenta, and their implications in various other exoticities of the material. In addition, we discover several other surface states at binding energies higher than the Dirac point, revealing the complexity of the system. Since the Rashba term alone cannot adequately capture the experimental results, we constructed a model Hamiltonian including spin-orbit coupling terms of higher order in momentum. Our model provides an excellent description of the anisotropy of the Dirac states. The necessity of the higher-order terms reveals the importance of the absence of inversion symmetry in the electronic properties of such systems.

ACKNOWLEDGMENTS

The authors acknowledge financial support from the Department of Atomic Energy, Government of India, under Project No. 12-R&D-TFR-5.10-0100, Diamond Light Source for beamtime at beamline I05 under Proposal No. SI11512. D.V.V. acknowledges support from the Spanish Ministry of Economy (No. MAT-2017-88374-P). K.M. acknowledges financial support from DAE, Government of India, under the DAE-SRC-OI Award program, and Department of Science and Technology, Government of India, under the J. C. Bose Fellowship program.

APPENDIX

The experimental geometry involving the sample orientation and the photoemission plane is discussed below. The angle θ_1 is defined as the azimuthal angle made by the vector, $\overline{\Gamma} - \overline{S}$, with the analyzer slit; the analyzer slit is aligned along the y direction. The tilt angle θ_2 is the angle between the analyzer and the sample-surface-normal. Depending on the magnitudes of θ_1 and θ_2, different trends of the energy gap at the Dirac node is expected as a function of probing photon energy.

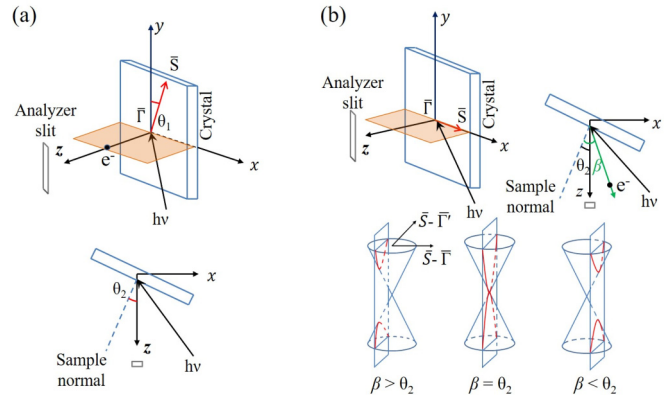

FIG. 7. Schematics of the experimental geometry. (a) The geometry used in the present study where θ_1 and θ_2 are in-plane (azimuthal) and out-of-plane (polar) angles, respectively. (b) A special case where the in-plane angle, $\theta_1 = 90°$. The angle β is the emission angle of photoelectrons corresponding to the Dirac node with respect to the sample surface-normal. Conic sections in the lower panel show the expected band dispersions in the spectra for different values of β with respect to θ_2 due to the change in photon energy keeping the sample orientation unchanged.

As an example, we consider a less complex scenario in Fig. 7(b); $\theta_1 = 90^o$ and $\theta_2 \neq 0$. Here the $\overline{\Gamma'} - \overline{S} - \overline{\Gamma'}$ vector lies along the slit (probed k vector). If the Dirac node is located at a finite momentum along the $\overline{\Gamma} - \overline{S}$ direction, corresponding electrons will emerge at an angle β with respect to the sample-normal. The magnitude of β depends on the photon energy used for experiments; with the increase of the photon energy, β will reduce. For sufficiently low photon energy, β will be larger than θ_2. It becomes equal to θ_2 at some photon energy and then becomes smaller at higher photon energies. The lower panel of Fig. 7(b) depicts the schematics of the acquired dispersion using a conic section. The vertical plane is the plane of constant momentum along $\overline{\Gamma} - \overline{S}$, which lies parallel to the analyzer slit. Intersection of this vertical plane and the cone determines the shape of the dispersion (red curves) as seen in the spectra. When $\beta \neq \theta_2$, instead of a cone the Dirac state manifests itself as two hyperbolas separated by an energy gap. An ideal cone with a Dirac node is imaged at a particular photon energy when the corresponding β becomes equal to θ_2. Earlier ARPES results can be captured excellently well using this description. As a representative case, we analyzed the ARPES data of Thirupathaiah *et al.* [6], exhibiting identical behavior for $\theta_2 = 9.6^o$ and $\theta_1 = 90^o$. If θ_1 is different from 0^o or 90^o, the cuts on the Dirac cone will not produce hyperbolas symmetrically aligned with respect to the vertical axis. This is the scenario in Figs. 2(a) and 2(b).

[1] H. Zhang, C. X. Liu, X. L. Qi, X. Dai, Z. Fang, and S. C. Zhang, Nat. Phys. **5**, 438 (2009).

[2] Y. L. Chen, J. H. Chu, J. G. Analytis, Z. K. Liu, K. Igarashi, H. H. Kuo, X. L. Qi, S. K. Mo, R. G. Moore, D. H. Lu, M. Hashimoto, T. Sasagawa, S. C. Zhang, I. R. Fisher, Z. Hussain, and Z. X. Shen, Science **329**, 659 (2010).

[3] D. Kong, J. J. Cha, K. Lai, H. Peng, J. G. Analytis, S. Meister, Y. Chen, H. J. Zhang, I. R. Fisher, Z. X. Shen, and Y. Cui, ACS Nano **5**, 4698 (2011).

[4] D. Biswas, S. Thakur, K. Ali, G. Balakrishnan, and K. Maiti, Sci. Rep. **5**, 10260 (2015); D. Biswas, S. Thakur, G. Balakrishnan, and K. Maiti, *ibid.* **5**, 17351 (2015); D. Biswas and K. Maiti, Europhys. Lett. **110**, 17001 (2015); J. Electron. Spectrosc. Relat. Phenom. **208**, 90 (2016).

[5] H. M. Benia, E. Rampi, C. Trainer, C. M. Yim, A. Maldonado, D. C. Peets, A. Stöhr, U. Starke, K. Kern, A. Yaresko, G. Levy, A. Damascelli, C. R. Ast, A. P. Schnyder, and P. Wahl, Phys. Rev. B **94**, 121407(R) (2016).

[6] S. Thirupathaiah, S. Ghosh, R. Jha, E. D. L. Rienks, K. Dolui, V. V. R. Kishore, B. Büchner, T. Das, V. P. S. Awana, D. D. Sarma, and J. Fink, Phys. Rev. Lett. **117**, 177001 (2016).

[7] M. Neupane, N. Alidoust, M. M. Hosen, J. X. Zhu, K. Dimitri, S. Y. Xu, N. Dhakal, R. Sankar, I. Belopolski, D. S. Sanchez, T. R. Chang, H. T. Jeng, K. Miyamoto, T. Okuda, H. Lin, A. Bansil, D. Kaczorowski, F. Chou, M. Zahid Hasan, and T. Durakiewicz, Nat. Commun. **7**, 13315 (2016).

[8] M. Sakano, K. Okawa, M. Kanou, H. Sanjo, T. Okuda, T. Sasagawa, and K. Ishizaka, Nat. Commun. **6**, 8595 (2015).

[9] L. A. Wray, S. Y. Xu, Y. Xia, Y. S. Hor, D. Qian, A. V. Fedorov, H. Lin, A. Bansil, R. J. Cava, and M. Z. Hasan, Nat. Phys. **6**, 855 (2010).

[10] Shruti, V. K. Maurya, P. Neha, P. Srivastava, and S. Patnaik, Phys. Rev. B **92**, 020506(R) (2015).

[11] C. Q. Han, H. Li, W. J. Chen, F. Zhu, M. Y. Yao, Z. J. Li, M. Wang, B. F. Gao, D. D. Guan, C. Liu, C. L. Gao, D. Qian, and J. F. Jia, Appl. Phys. Lett. **107**, 171602 (2015).

[12] B. Joshi, A. Thamizhavel, and S. Ramakrishnan, Phys. Rev. B **84**, 064518 (2011).

[13] M. Mondal, B. Joshi, S. Kumar, A. Kamlapure, S. C. Ganguli, A. Thamizhavel, S. S. Mandal, S. Ramakrishnan, and P. Raychaudhuri, Phys. Rev. B **86**, 094520 (2012).

[14] Z. Sun, M. Enayat, A. Maldonado, C. Lithgow, E. Yelland, D. C. Peets, A. Yaresko, A. P. Schnyder, and P. Wahl, Nat. Commun. **6**, 6633 (2015).

[15] A. Yaresko, A. P. Schnyder, H. M. Benia, C. M. Yim, G. Levy, A. Damascelli, C. R. Ast, D. C. Peets, and P. Wahl, Phys. Rev. B **97**, 075108 (2018).

[16] M. Hoesch, T. K. Kim, P. Dudin, H. Wang, S. Scott, P. Harris, S. Patel, M. Matthews, D. Hawkins, S. G. Alcock, T. Richter, J. J. Mudd, M. Basham, L. Pratt, P. Leicester, E. C. Longhi, A. Tamai, and F. Baumberger, Rev. Sci. Instrum. **88**, 013106 (2017).

[17] Y. L. Chen, J. G. Analytis, J. H. Chu, Z. K. Liu, S. K. Mo, X. L. Qi, H. J. Zhang, D. H. Lu, X. Dai, Z. Fang, S. C. Zhang, I. R. Fisher, Z. Hussain, and Z.-X. Shen, Science **325**, 178 (2009).

[18] S. Souma, K. Kosaka, T. Sato, M. Komatsu, A. Takayama, T. Takahashi, M. Kriener, K. Segawa, and Y. Ando, Phys. Rev. Lett. **106**, 216803 (2011).

[19] K. Kuroda, M. Arita, K. Miyamoto, M. Ye, J. Jiang, A. Kimura, E. E. Krasovskii, E. V. Chulkov, H. Iwasawa, T. Okuda, K. Shimada, Y. Ueda, H. Namatame, and M. Taniguch, Phys. Rev. Lett. **105**, 076802 (2010).

[20] T. Valla, Z. H. Pan, D. Gardner, Y. S. Lee, and S. Chu, Phys. Rev. Lett. **108**, 117601 (2012).

[21] Q. D. Gibson, D. Evtushinsky, A. N. Yaresko, V. B. Zabolotnyy, M. N. Ali, M. K. Fuccillo, J. Van den Brink, B. Büchner, R. J. Cava, and S. V. Borisenko, Sci. Rep. **4**, 5168 (2014).

[22] G. Autès, A. Isaeva, L. Moreschini, J. C. Johannsen, A. Pisoni, R. Mori, W. Zhang, T. G. Filatova, A. N. Kuznetsov, L. Forró, W. V. den Broek, Y. Kim, K. S. Kim, A. Lanzara, J. D. Denlinger, E. Rotenberg, A. Bostwick, M. Grioni, and O. V. Yazyev, Nat. Mater. **15**, 154 (2015).

[23] F. Virot, R. Hayn, M. Richter, and J. van den Brink, Phys. Rev. Lett. **106**, 236806 (2011).

[24] W. Zhang, R. Yu, W. Feng, Y. Yao, H. Weng, Xi Dai, and Z. Fang, Phys. Rev. Lett. **106**, 156808 (2011).

[25] R. Requist, P. M. Sheverdyaeva, P. Moras, S. K. Mahatha, C. Carbone, and E. Tosatti, Phys. Rev. B **91**, 045432 (2015).

[26] L. Fu, Phys. Rev. Lett. **103**, 266801 (2009).

[27] C. X. Liu, X. L. Qi, H. Zhang, X. Dai, Z. Fang, and S. C. Zhang, Phys. Rev. B **82**, 045122 (2010).

[28] Estimated parameters (units = eV, $Å^{-1}$) found for the description of the dispersion and contours: $E_0 = -0.66$, $c_{13} = -1.49$, $c_{14} = -0.48$, $c_{15} = 0$, $c_1^2 + c_7^2 = 0.21$,

$c_1c_2 + c_7c_8 = 0$, $c_2^2 + c_8^2 = 0.30$, $c_1c_5 + c_7c_{11} = -5.45$, $c_1c_4 + c_7c_{10} + c_2c_5 + c_8c_{11} = 0$, $c_1c_3 + c_7c_9 + c_2c_4 + c_8c_{10} = -1.38$, $c_1c_6 + c_7c_{12} + c_2c_3 + c_8c_9 = 0$, $c_2c_6 + c_8c_{12} = -2.13$, $c_5^2 + c_{11}^2 = 73.67$, $c_4c_5 + c_{10}c_{11} = 0$, $c_4^2 + c_{10}^2 + 2c_3c_5 + 2c_9c_{11} = 50.6$, $c_3c_4 + c_9c_{10} + c_5c_6 + c_{11}c_{12} = 0$, $c_3^2 + c_9^2 + 2c_4c_6 + 2c_{10}c_{12} = -21.6$, $c_3c_6 + c_9c_{12} = 0$, $c_6^2 + c_{12}^2 = 14.97$.

[29] A. Pramanik, R. P. Pandeya, K. Ali, B. Joshi, I. Sarkar, P. Moras, P. M. Sheverdyaeva, A. K. Kundu, C. Carbone, A. Thamizhavel, S. Ramakrishnan, and K. Maiti, Phys. Rev. B **101**, 035426 (2020).

[30] M. Nomura, S. Souma, A. Takayama, T. Sato, T. Takahashi, K. Eto, K. Segawa, and Y. Ando, Phys. Rev. B **89**, 045134 (2014).

[31] D. Yu. Usachov, I. A. Nechaev, G. Poelchen, M. Güttler, E. E. Krasovskii, S. Schulz, A. Generalov, K. Kliemt, A. Kraiker, C. Krellner, K. Kummer, S. Danzenbächer, C. Laubschat, A. P. Weber, J. Sánchez-Barriga, E. V. Chulkov, A. F. Santander-Syro, T. Imai, K. Miyamoto, T. Okuda, and D. V. Vyalikh, Phys. Rev. Lett. **124**, 237202 (2020).